Design of an Integrated Microvascularised Human Skin-on-a-Chip Tissue Equivalent Model

Christian F. E. Jones[1,2], Stefania di Ciò[1,2], John Connelly[3], Julien Gautrot[1,2*]

[1]Institute of Bioengineering and [2]School of Engineering and Materials Science, Queen Mary University of London, London, United Kingdom

[3]The Blizard Institute, Queen Mary University of London, London, United Kingdom

*** Correspondence:**
Julien Gautrot
j.gautrot@qmul.ac.uk

Keywords: organ-on-a-chip, microfluidics, microvascularisation, soft lithography, vasculogenesis.

Abstract

Tissue engineered skin constructs have been under development since the 1980s as a replacement for human skin tissues and animal models for therapeutics and cosmetic testing. These have evolved from simple single cell-assays to increasingly complex models with integrated dermal equivalents and multiple cell types including a dermis, epidermis and vasculature. The development of micro-engineered platforms and biomaterials has enabled scientists to better recreate and capture the tissue microenvironment in vitro, including the vascularization of tissue models and their integration into microfluidic chips. However, to date, microvascularised human skin equivalents in a microfluidic context have not been reported. Here we present the design of a novel skin-on-a-chip model integrating human derived primary and immortalized cells in a full thickness skin equivalent. The model is housed in a microfluidic device, in which a microvasculature was previously established. We characterize the impact of our chip design on the quality of the microvascular networks formed and evidence that this enables the formation of more homogenous networks. We developed a methodology to harvest tissues from embedded chips, after 14 days of culture, and characterize the impact of culture conditions and vascularization (including with pericyte co-cultures) on the stratification of the epidermis in the resulting skin equivalents. Our results indicate that vascularization enhances stratification and differentiation

(thickness, architecture and expression of terminal differentiation markers such as involucrin and transglutaminase 1), allowing formation of more mature skin equivalents in microfluidic chips. The skin-on-a-chip tissue equivalents developed, thanks to their realistic microvasculature, may find application for the testing efficacy and safety of therapeutics delivered systemically, in a human context.

1 Introduction

Our ability to recreate more complex tissue structure and function has considerable improved. As the fields of micro-engineering and biomaterials science developed, it has become increasingly clear that recreating some of the 3D architecture of tissues may be essential to reproduce the cell microenvironment and direct cell phenotype and tissue structure or function. Dating back from the 80s, micro-engineered platforms allowed the control of single cell adhesion and patterning, in turn allowing to control their phenotype (Watt et al., 1988, Chen et al., 1997, Connelly et al., 2010, Tan et al., 2013). More recently, the formation of clusters allowing to capture more complex behaviors, including cell segregation, motility, sprouting and differentiation have been developed (Nelson et al., 2006, Ruiz and Chen, 2008, Gautrot et al., *2012,* Costa et al., 2014). However, these platforms remained inherently based on 2D models, certainly relevant to cells forming 2D assemblies such as epithelia, but clearly limiting the creation of more complex architectures. Although interesting strategies were proposed to bridge the 2D and 3D world (Bosch-Fortea et al., 2019), making use of 2D patterns to guide cell-assembly in a 3D matrix, our ability to micro-engineer 3D tissues required the development of novel platforms.

The field of skin biology was certainly the first to see striking progress in the development of complex hierarchical tissue structures, with stratified differentiated skin equivalents of human tissues forming from epidermal keratinocytes assembling as monolayers at the surface of hydrogels encapsulating fibroblasts (Shahabeddin et al., 1990, Stark et al., 2006). This allowed not only the recreation of well-

49 differentiated human skin equivalents, but also allowed capturing some of the skin barrier functions,
50 from trans-epithelial resistance to the diffusion of therapeutics and nanomaterials (Ackermann et al.,
51 2010, Asbill et al., 2000, Bellas et al., 2012, Mazlyzam et al., 2007). These include models which have
52 integrated other *in vivo* skin structures and cell types including the hair follicle (Langan et al., 2015) and
53 melanocytes (Li et al., 2011, Liu et al., 2007). More recently, a broad range of tissues have beneficiated
54 from advances in stem cell biology, spheroid and organoid models and progress in biomaterials and
55 microfabrication. This ranges from the formation of functional muscle and lung tissue models (Huh et
56 al., 2010, Ronaldson-Bouchard et al., 2018, Sakar et al., 2016) to the development of complex organoid
57 models, for example of gut, skin and brain tissues (Lancaster et al., 2013, Lee et al., 2020).

58 As tissues grew in complexity and size, vascularization became an important hurdle, either to their further
59 development or growth, or simply their long term survival and applicability (Baish et al., 2011, Coloma
60 et al., 1997, Colton, 1995). In addition, recapitulating the complex architecture and function of
61 microvascularised tissues will be important to the accurate prediction of therapeutics safety and efficacy
62 (Loskill et al., 2021) for example mimicking systemic delivery to targeted tissues. To address this issue,
63 a range of tissue models have been placed in parallel with endothelialised structures, therefore allowing
64 to recreate the endothelium-tissue interface. This has in particular be exploited in a broad range of tissue-
65 on-chip models, using porous membranes to separate an endothelial compartment from a tissue
66 compartment (Hassell et al., 2017, Huh et al., 2010, Kilic et al., 2016, Kim and Ingber, 2013). In addition
67 to simply structuring tissues, this approach enables the mechanical stimulation of resulting tissues, an
68 important factor regulating cell and tissue biology and response to pathogen or during disease
69 progression. In order to recreate more functional models of vessels, a range of platforms have been
70 engineered to allow the endothelialization of micro-capillaries and microchannels, allowing to study
71 phenomena such as sprouting and angiogenesis in more realistic scenarios (Liu et al., 2021, Menon et
72 al., 2017, Trappmann et al., 2017).

73 Increasingly, microvascularised models have become popular, as enabling to accurately capture the
74 architecture and function of microvascular networks perfusing tissues (Polacheck et al., 2014). Early
75 work from Kamm and co-workers and Jeon et al. showed that microvascular networks can conveniently
76 be assembled and maintained in microfluidic chips, allowing the formation of perfusable capillaries
77 (Galie et al., 2014, Kim et al., 2013). Such models can be derived through angiogenesis, from
78 endothelialised microchannels interfaces with hydrogel compartments separated by micro-posts, or by
79 direct assembly of networks via vasculogenesis, therefore enabling faster formation of functional
80 structures. Subsequently, hydrogel compartment were loaded with stem cells and disease cell lines in
81 order to recreate vascularized tissue models (Chen et al., 2017, Jeon et al., 2015, Kim et al., 2015a).
82 Another attractive alternative proposed consists in placing spheroids, and in some cases organoids within
83 wells designed within the hydrogel compartment, therefore enabling the vascularization of resulting
84 tissue models (Homan et al., 2019, Ko et al., 2019a, Shin et al., 2021, Sobrino et al., 2016). Although
85 this remains moderately successful for the interpenetration of organoids, this strategy has been
86 particularly promising for spheroid models.

87 The field of skin biology has seen the development of a range of skin equivalents interfaced with
88 endothelial models. For example, endothelial barriers were formed at the bottoms or back of dermal
89 compartments of human skin equivalents (Kwak et al., 2020, Lee et al., 2017, Wufuer et al., 2016)
90 including in microfluidic chips, and micro-capillaries were allowed to assemble at the bottom of dermal
91 constructs in transwell systems (Black et al., 1998, (Schurr et al., 1999) Such models of skin
92 vascularization displayed improved epidermal barrier function (Kim et al., 2019, Kwak et al., 2020) and
93 basal cell proliferation and differentiation (Kim et al., 2019), compared to non-endothelialised
94 equivalents. However, few successful vascularized skin-equivalent models, integrated into microfluidic
95 chips, have been reported to date.

96 In this report, we present the design of a full thickness human skin-on-a-chip model displaying a stratified
97 differentiated epidermal compartment, assembled above a microvascularised dermal compartment
98 (Figure 1). We first design a novel microfluidic chip featuring a circular central chamber separated from
99 circumferential channels by micro-posts and characterize the impact of such structure on the morphology
100 of the microvasculature. We then first identify culture conditions suitable for the formation of a stratified
101 human skin equivalent in the resulting chips, prior to evaluating the impact of vascularization of the
102 resulting tissue structure and epidermal differentiation. In addition, we introduce pericytes in the vascular
103 compartment, in order to stabilize associated structures and evaluate the impact of such co-culture on the
104 resulting vascularized skin equivalents. Overall, our results demonstrate the formation of vascularized
105 skin-on-chip models that could be scaled and parallelized in order to design high throughput platforms
106 for the testing of safety and efficacy of therapeutics.

107 **2 Materials and Methods**

108 **2.1 Chip Design and Manufacture**

109 Chips were designed in AutoCAD by AutoDesk and printed on acetate sheets by Micro Lithography
110 Services, Chelmsford, UK. Microfluidic chips were generated using Sylgard™ 184 PDMS and glass
111 coverslips, following literature protocols (Jenkins, 2013). In short, masters were manufactured by
112 coating clean silicon wafers with a negative photo resist (SU-2050) using a spin coater set to 500 rpm
113 for 10 seconds (ramp 100 rpm/second for the initial 5 seconds) to distribute the photoresist, followed by
114 a spin speed of 1700 rpm for 30 seconds (ramp 300 rpm/second for the initial 4 seconds) to spread the
115 resist to a uniform depth of 80 µm. After an initial soft bake at 65°C for 3 min and then at 95°C for 10
116 min to harden the surface of the photoresist, photomasks corresponding to the desired chip micro-
117 architectures were placed on the surface of the wafer and photocured with UV light at 90 mW/cm^2 for
118 2.4 s, allowing resist crosslinking to occur. Resists were post-baked at 65°C for 3 min and then at 95°C

119 for 10 min to assist the crosslinking, allowing to rest in between, then immersed in propylene glycol
120 methyl ether acetate (PGMEA, Sigma Aldrich, 484431) for 5 minutes to dissolve un-crosslinked
121 photoresist. Masters were immediately rinsed in isopropanol to remove excess PGMEA and dried under
122 a stream of nitrogen. The resulting masters were examined using a reflected light microscope to confirm
123 suitable patterning, and then incubated at 150°C for 3 min to hard bake the photoresist.. The PDMS base
124 (Sylgard™ 184) was mixed with its curing agent at a 10:1 ratio, after which air bubbles were removed
125 via centrifugation or under vacuum. The resulting formulation was poured onto the masters to a depth of
126 5 mm, placed under vacuum again to eliminated bubbles, and then left overnight at 70°C to allow full
127 curing. The PDMS blocks were cut away from the masters to produce a stamp with features
128 corresponding to the microarchitecture of the master. Biopsy punches were used to introduce cell culture
129 medium reservoirs and hydrogel inlets, which can then be cleaned with residue free tape to remove any
130 obvious debris and rinsed in deionized water and isopropanol or ethanol before drying in nitrogen. The
131 stamps were placed in an air plasma system (HPT-200, Henniker Plasma) and treated for one minute
132 with the channels facing upward, alongside glass coverslips. The PDMS blocks were then rapidly pushed
133 firmly against the coverslip for 30 s to allow bonding and each chip was carefully inspected to ensure the
134 system was fully sealed. Finally, chips were autoclaved and left in an oven for at least 48 h to allow the
135 PDMS to recover its hydrophobicity.

136 **2.2 Cell Culture**

137 All primary cells used as part of this project were between passage numbers 3-6. Cells were cultured in
138 T75 Nunc™ EasYFlask™ cell culture flasks (ThermoFisher®, 156499) at 37°C and 5% CO_2 and
139 passaged at approximately 80% confluency. HUVECs were obtained from Lonza™ and cultured in
140 Endothelial Cell Growth Medium-2 (EGM-2, PromoCell® C-22111 or Lonza™ CC-3162). Human
141 primary pericytes were purchased from PromoCell® (PromoCell®, C-12980) and cultured in Pericyte
142 Growth Medium-2 (PGM2) also from PromoCell® (PromoCell®, C-28041). Detachment was achieved

143 using a pericyte detachment kit (PromoCell®, C-41200), requiring addition of 5 mL HEPES buffered
144 saline solution to the cells for washing, after medium aspiration, aspiration and addition of 5 mL
145 Trypsin/EDTA 0.04%/0.03% for 3 min at room temperature. Trypsinisation was inhibited by addition of
146 5 mL trypsin neutralization solution, after which cells were centrifuged and resuspended in PGM2.

147 HCA2 fibroblasts - a human telomerase reverse transcriptase (hTERT) immortalized human dermal
148 fibroblast cell line (Stephens et al., 2004) were cultured in Dulbecco's modified Eagle medium (DMEM,
149 Gibco™*)* supplemented with 10% fetal bovine serum (FBS, Gibco™ 26140079), 1% L-Glutamine and
150 1% penicillin-streptomycin (PS, Gibco™ 15140122). N/TERT cells (Hahn et al., 2000), a human
151 keratinocyte cell line featuring constitutive expression of human telomerase reverse transcriptase
152 (hTERT) were cultured in FAD medium (3:1 DMEM : Ham's F12 Medium (ThermoFisher®,
153 11320074), supplemented with 1% PS, 1% L-Glutamine, 10% FBS, 0.5 µg/mL human hydrocortisone
154 (Fisher Scientific®, 35245-0010), 8.47ng/ml cholera toxin (Sigma-Aldrich®, C8052-1mg), 10 ng/mL
155 human epidermal growth factor (Peprotech®, AF-100-15) and 5 µg/mL human insulin (Sigma-Aldrich®,
156 15500).

157 **2.3 Vasculogenesis Assays**

158 A bovine fibrin gel was used as a matrix for vascularization, following protocols reported in the literature
159 (Rohringer et al., 2014). In short, lyophilized bovine fibrinogen (Sigma-Aldrich®, F8630-25G) was
160 dissolved in dPBS to a concentration of 20 mg/mL and filtered to ensure sterility. Separately, a bovine
161 thrombin solution of 4 U/mL was prepared by dissolving lyophilized bovine thrombin derived from
162 bovine plasma (Sigma-Aldrich, T4648-1KU) in 0.1% bovine serum albumin solution (BSA, Sigma-
163 Aldrich, A9418-50G) in dPBS, which was added to EGM-2 to achieve the final concentration. Prior to
164 injection into the device, 20 µL aliquots of fibrinogen solution were mixed with equal volumes of

165 thrombin solution in which was suspended appropriate densities of HUVECs, which triggered formation
166 of the final gel encapsulating endothelial cells.

167 For both chip designs, the wide central chamber was filled with 10 μL of a fibrin gel with a concentration
168 of 10 mg/mL, in which HUVECs were suspended at a density of 6-10 million cells/mL by injection
169 through the 3 mm central well with a cut 20 μL pipette tip. Both side channels were filled with EGM-2
170 supplemented with 50 ng/mL Vascular Endothelial Growth Factor (VEGF) through filling individual
171 wells at one end of the chip and applying a negative pressure to the corresponding well for each channel
172 using a 1000 μL pipette, therefore allowing channel perfusion. Medium reservoirs were filled equally.
173 Chips were left to incubate at 37°C for approximately 45 min whilst HCA2 cells were passaged and
174 encapsulated in a collagen gel at a density of 2 million cells/mL. Collagen gels were formed using rat-
175 tail derived collagen I, as follows: working over ice, aqueous NaOH (1M) was added to 10X dPBS
176 (ThermoFisher®, 70011044). Rat tail derived type I collagen (Corning®, 354249) was added to the
177 buffer solution followed by HCA2 cells in dPBS and the mixture was well mixed, resulting in a final
178 collagen concentration of 5 mg/mL and a HCA2 density of 2 million cells/mL. 30 μL of collagen gel
179 solution containing fibroblasts was placed into the central well and allowed to set upon the HUVECs-
180 loaded fibrin gel cast at the bottom. Medium wells and the central well were filled with EGM2 containing
181 additional 50 ng/mL VEGF. Medium was replaced daily and after one week of culture were fixed in 4%
182 PFA in PBS and stained for imaging.

183 **2.4 Organotypic Skin-on-a-Chip Formation and Vascularization**

184 **2.4.1 Dermal Equivalent preparation**

185 Fibrin gels were prepared and injected into the vascular compartment of chips, either without cells, at
186 10^7 cells/mL HUVECs or 10^7 cells/mL HUVECs and 10^6 cells/mL pericytes. 20 μL was injected into
187 each chip. For vascularized chips, devices were filled with EGM-2 containing additional 50 ng/mL

188 VEGF, which was replaced daily and cultured for 4 days before addition of the dermal and epidermal
189 equivalents, to allow vascular development. Avascular chips were incubated with VEGF supplemented
190 EGM2 24 h before addition of the skin equivalent. For embedding of the dermal equivalent gel precursor,
191 solutions were stored on ice, using pre-cooled pipette tips kept in sterile sealed boxes at 0°C and
192 microcentrifuge tubes to avoid premature Matrigel ® setting. Medium was removed from the reservoirs
193 and central well of the devices. 250 µL high concentration (9 mg/mL) rat-tail derived collagen I solution
194 was injected into a microcentrifuge tube, followed by 100 µL Matrigel ® (Corning®, 356234) and 50
195 µL 10X DMEM (ThermoFisher®, 11430030). After thorough mixing to ensure homogeneity, the pH
196 was adjusted to 7 by dropwise addition of sterile 1 M NaOH, in aliquots of 5 µL, followed by further
197 mixing, to a volume of approximately 405 µL. 50 µL sterile FBS was added and mixed in, and the
198 mixture was put aside on ice until primary fibroblasts had been passaged and re-suspended to 1 M/mL in
199 complete DMEM. 50 µL cell suspension was added to the collagen/Matrigel ® mixture and mixed
200 thoroughly to a final fibroblast density of 10^5 cells/mL. 20 µL of the resulting cell suspension in gel
201 precursor mixture was injected into the central well of the device atop the fibrin scaffold. Injection was
202 carried on the sides of the well, to avoid the formation of bubbles allowing the matrix to rest evenly
203 across the surface of the fibrin gel underneath and to fill the entire diameter of the well.

204 **2.4.2 Epidermal Equivalent Preparation**

205 Chips were incubated at 37°C for 1 h to allow gels to set, followed by passage of N/TERTs by addition
206 of 10 mL sterile versene solution for 5 min followed by addition of 2 mL sterile 0.05% trypsin-EDTA
207 for 5 min at 37°C. Cells were re-suspended to 10^6 cells/mL in FAD and 25 µL of the suspension was
208 injected on top of the gel down the side of the central well, to avoid bubble formation. After 10 min of
209 incubation at room temperature to allow N/TERT attachment to the top of the dermal equivalent, the
210 central well and medium wells were filled with FAD and chips were cultured overnight at 37°C and 5%

211 CO_2. After approximately 18 h of incubation, medium was aspirated from the chips and fresh FAD
212 medium was replaced, which was done daily over the culture period. Chips were cultured for 7-14 days
213 at 37°C and 5% CO_2 before fixation in 4% PFA.

214 **2.5 Imaging**

215 **2.5.1 On-Chip Immunological Staining**

216 For samples that were imaged on-chip, fixation was carried out in 4% PFA in PBS for 15 min, followed
217 by washing in PBS thrice and incubated in 0.2% triton-X for 15 min. Primary and subsequently secondary
218 stains were applied in 3% BSA overnight followed by a PBS wash. Chips were loaded whole into a
219 sample holder mounted to the stage of the Zeiss™ LSM710 confocal microscope and imaged.

220 **2.5.2 Histology**

221 **2.5.2.1 Cryo-Histological Sectioning**

222 For sectioning, immunostaining and confocal imaging, after fixation, samples were immersed in 30%
223 sucrose solution in PBS overnight by injection into lateral medium wells and the central well. This was
224 aspirated the following day and replaced with a 10% sucrose/ 7.5% porcine gelatin solution in PBS and
225 chips were left at 37°C for 15 min to allow the matrix to set. Simultaneously, some of the gelatin solution
226 was carefully pipetted into well plates avoiding bubble formation to a depth of approximately 1 cm, and
227 the plates were left at 4°C for 15 min to allow the matrix to set. Tissues were harvested from the central
228 wells of the chips by slicing the coverslip from the PDMS carefully with a sharp scalpel and cutting
229 chunks from the remaining block until the organotypic was exposed on 3 sides. At this point, the cultures
230 were scooped from the PDMS and laid atop the set gels in well plates. More gelatin solution was injected
231 to immerse the cultures completely and the well plates were placed back at 4°C for 15 min to set. A cold
232 hexane bath was made by dropping pieces of dry ice into hexane in a deep glass dish with thick sides

233 until it reached a temperature of between -30°C and -50°C. Orientation of the blocks was assured by
234 cutting the corners of the blocks to be attached to the sample holder of the cryostat. Samples were frozen,
235 sectioned and stored at -80°C until ready for staining.

236 **2.5.2.2 Paraffin Embedded Section De-Waxing and Antigen Unmasking**

237 Redundant human skin was obtained from healthy donors following plastic surgery procedures at the
238 Royal London Hospital or Phoenix Hospital, Essex. All donors provided written informed consent
239 according to local ethical approval (East London Research Ethics Committee, study number 2011-
240 000626-29 and East of England Research Ethics Committee, study number 21/EE/0057). Human skin
241 sections embedded in paraffin wax were dewaxed by incubation at 55°C for 10 min to melt the paraffin
242 followed by immersion in xylenes thrice, each for 15 min. To rehydrate the sections, slides were left in
243 a bath of ethanol and xylenes at a 1:1 ratio for 5 min, followed by sequential incubation in 100%, 95%
244 and 70% ethanol in deionized water, and finally pure deionized water (all twice, each for 2 min). To
245 unmask antigens hidden during sample fixation, the deionized water was aspirated and sections were
246 immersed in a 0.05% trypsin/0.1% $CaCl_2$ solution in deionized water, pre-warmed to 37°C, and were
247 incubated in a humid box for 20 min at 37°C. Samples were washed thrice more with dPBS before
248 staining.

249 **2.5.2.3 Section Staining & Slide Preparation**

250 Prior to staining, sections were allowed to equilibrate to room temperature for around 2 h. Sections were
251 outlined with a hydrophobic pen to facilitate staining and reduce volumes of required reagents. 4% PFA
252 in PBS was dropped onto each section for 15 min, followed by a PBS wash and further 15 min incubation
253 with 0.2% triton-X in PBS. Following another PBS wash, sections were blocked overnight in 3% BSA
254 solution in PBS at 4°C to reduce the risk of dehydration. Sections were incubated with 15 µL primary
255 antibody solution overnight in 3% BSA at 4°C, according to the stain required. These included antibodies

256 with the following antigens: keratin 14 (K14, AbCam® ab192055, 1:250), Involucrin (ThermoFisher®,
257 MA511803, 1:40), Ki67 (RM9106-50, 1:125), laminin-332 (AbCam®, ab14509, 1:250), vimentin
258 (AbCam®, ab8978, 1:150), TGM-1 (SigmaAldrich®, HPA040171, 1:150) and CD31 (BioLegend®,
259 303126, 1:100). Secondary antibodies were also applied overnight in a 3% BSA solution in PBS
260 frequently alongside rhodamine-phalloidin and DAPI. These were Invitrogen® antibodies purchased
261 from ThermoFisher® attached to AlexaFluor™ fluorophores with emission wavelengths of 488 nm or
262 647 nm. Secondary antibodies were raised against antigens according to the animal origins of the primary
263 antibodies and diluted 1:1000.

264 Sections were washed with PBS which was carefully aspirated, followed by addition of Fluoromount-
265 G™ Mounting Medium (ThermoFisher®, 00-4958-02) and a coverslip. Coverslips were allowed to
266 attach at room temperature overnight and slides were carefully cleaned with ethanol prior to imaging.
267 All fluorescent imaging was performed with the Zeiss™ LSM710 Confocal microscope.

268 **2.6 Image & Statistical Analysis**

269 For microvessel analysis, Z-stack files were loaded into Fiji and flattened to produce an image across the
270 depth of the microvascularised compartment. These were analyzed in AngioTool (Zudaire et al., 2011)
271 to find vessel junction number, overall vessel length and percentage area covered in any given image by
272 vasculature. To analyze sections, Z-Stacks were taken through the entire depth of sections and loaded
273 into Fiji. Individual slices were taken from the central image of each stack as representative of that stack
274 and used for data acquisition and figure production. Statistical analyses were carried out using SPSS by
275 IBM.

276

277

278 **3. Results**

279 **3.1 Vasculogenesis-on-a-Chip**

280 The proposed design of the microvascularised chip (Figure 1) is based on three channel chips previously
281 reported by Kamm, Jeong and others (Hernández Vera et al., 2008, Jeon et al., 2014). In these
282 microfluidic systems, three parallel linear channels are separated by micro-posts that can vary
283 significantly in size and shape from one report to another. This enables the central channel to be loaded
284 with an endothelial cell suspension in a gel precursor solution that is allowed to set *in situ* prior to filling
285 the side channels with tissue culture medium. The device initially selected featured a hexagonal
286 microfluidic chamber, 5 mm wide, with an integrated 3 mm diameter circular central well open to the
287 air, allowing a minimal gap of 1 mm between the circumference of the well and the edge of the chamber.
288 Peripheral medium channels were separated from the central chamber by 2 parallel series of hexagonal
289 posts, 380 μm long and 90 μm wide, either side of the microfluidic culture compartment. The
290 morphology and homogeneity of vascular networks formed in such systems were first investigated.

291 Vascularization was achieved via a vasculogenesis protocol adapted from the literature (Kim et al., 2016),
292 consisting in de novo capillary formation of HUVECs encapsulated within the fibrin gel in the central
293 compartment. The impact of cell density on vascular network formation was first examined
294 (Supplementary Figure S1). HUVECs were introduced in the central gel compartment at 6, 8 and 10
295 million cells/mL. After 7 days of culture, cells formed interconnected vascular networks that were
296 luminated, as evidenced by confocal microscopy (Figure 2). Cell densities had no significant impact on
297 the morphology of the networks formed, within the range tested (Supplementary Figure S1). The total
298 cross-section area of networks, the total length of capillaries and their degree of branching were
299 comparable. However, we noted that the quality of the networks differed significantly depending on their
300 position within the channel. Close to the central well (position A), vascular networks were denser (higher

301 cross-section areas, length and branching densities) than in more distant areas, close to the injection
302 channels (position B, Figure 2D-F).

303 To encourage more uniform vascularization, the device was redesigned. The hexagonal microfluidic
304 culture compartment flanked by straight parallel peripheral medium channels was replaced with a round
305 compartment with circumferential 1 mm wide channel (Figure 2B). Hexagonal posts were redesigned to
306 follow the circumference of the central channel. Given the lack of impact of HUVEC density on
307 vascularization, within the range tested, cells were seeded within these redesigned chips at a density of
308 8 million cell/mL (suspended in 10 mg/mL fibrin gel).

309 Vascularization surrounding the central channel of round chips was comparable to hexagonal chips
310 (Figure 2C-F), without significant changes in vascular network coverage, density or branching. In
311 contrast to what had been observed with hexagonal chips, comparison of images taken near the central
312 well of round chips with those taken near injection channels revealed no significant difference in network
313 architecture either (Figure 2D-F). Levels of coverage by vascular networks were comparable near the
314 central well and injection channels, and associated vascular networks were as dense and branched. This
315 suggests that improved medium diffusion in different compartment within round chips enables improved
316 formation of homogenous vascular networks. Examination of confocal z-stacks taken of corresponding
317 vascular compartments also indicated the formation of a lumenated structures (20 μm of internal
318 diameter) in networks formed in round chips (Figure 2G-H). Therefore our data indicate that round chips
319 support the growth of a mature and more homogenous microvascular networks within multi-
320 compartment microfluidic chips. This model was therefore adopted for the development vascularized
321 skin-on-a-chip systems.

322 **3.2 Establishment of a Skin-on-a-Chip Model**

323 To engineer the full thickness dermal equivalent within our microfluidic model, we proposed to introduce
324 dermal fibroblasts within the central well of round chips. As a first step, we introduced the dermal
325 compartment on top of an acellular fibrin gel, which could subsequently be vascularized, as presented in
326 Figures 1 and 2. A collagen I/Matrigel dermal equivalent matrix was selected, based on protocols
327 established for transwell skin equivalent culture (Enjalbert et al., 2020). Fibrin was injected into the
328 microfluidic compartment of the chip and devices were incubated at 37°C for 5 min, followed by
329 perfusion of medium channels and filling of all on-chip wells with complete DMEM. Chips were left for
330 24 h at 37°C to allow bubbles forming at the medium-hydrogel interface to disperse. The medium was
331 then removed from chips and 20 µL of dermal equivalent matrix (rat-tail derived collagen I and Matrigel
332 with pH adjusted to 7) together with 10^5 cells/mL primary human dermal fibroblasts were injected in the
333 central well and allowed to set at the surface of the fibrin compartment, for 1 h at 37°C. N/TERT
334 keratinocytes were passaged and resuspended at 1 million cells/mL in FAD medium, and 25 µL of the
335 suspension was injected on top of the dermal equivalent. Devices were incubated for 10 min at room
336 temperature to facilitate initial N/TERT attachment, followed by the filling of medium wells with FAD
337 medium. After 24 h incubation, the medium was removed from the chip and replaced. To examine the
338 impact of air-liquid interface culture, which is typically used for the formation of skin equivalents to
339 encourage epidermal stratification and differentiation, dermal equivalents on chips were either left
340 submerged (fresh FAD introduced into the central well) or exposed to air. Culture was continued for a
341 total of 7 or 14 d, followed by fixation and embedding for histology and immunological staining.

342 At day 7, keratinocytes formed confluent epidermal layers across the surfaces of dermal matrices and
343 positive for basal K14 (Supplementary Figure S2). After 14 days of culture, both in submerged conditions
344 and at the air-liquid interface, we observed the formation of confluent stratified epidermal layers, atop
345 the dermal equivalent matrix (Supplementary Figure S2). Infrequent proliferative cells (Ki67 positive)
346 were observed in the basal epidermal layers of epidermal equivalents cultured submerged in medium

347 (Figure 3). Although this localization and such overall low rates are typical of skin equivalents and
348 proliferation rates observed in vivo (Heenen et al., 1998, Commandeur et al., 2012), the lack of Ki67
349 positive cells in tissues formed at the air-liquid interfaces was surprising. In agreement with such
350 observations, we also observed significantly thicker epidermal equivalents in submerged cultures (46 +/-
351 16 μm) compared to those formed at the air-liquid interface (24 +/- 12 μm, Figure 3C). In addition, the
352 abundance of the basement membrane protein laminin-332 was significantly higher in submerged
353 cultures (by a factor of >2 fold, Figure 3C), suggesting that keratinocytes in these cultures were also
354 more active at remodeling corresponding interfaces and recreating a normal functional basal lamina. The
355 thickness of the basal marker keratin 14 was also significantly increased in submerged cultures (28 +/-
356 10 μm) compared to those kept at air-liquid interfaces (15 +/- 10 μm, Figure 4). Finally, whilst expression
357 of the terminal differentiation marker involucrin was observed in the upper-epidermal layers of both
358 cultures, the thickness of the associated differentiated layer was significantly increased in submerged
359 cultures (3.5 +/- 2.2 μm) compared to those kept at the air-liquid interface (0.5 +/- 0.2 μm, Figure 4).
360 However, relatively weak expression of the dermal fibroblast marker vimentin was observed in the
361 dermal compartment of both cultures, and very weak staining for the epidermal differentiation marker
362 transglutaminase 1 (TGM-1) was observed in the stratified layers of corresponding epidermal
363 compartments (Figure 4B).

364 **3.3 Microvascularised Skin-on-a-Chip Model**

365 The microvascularised model developed in a fibrin matrix, and the stratified human skin equivalent were
366 then combined in round chips. In addition, owing to their impact on the maturation and stabilization of
367 microvasculatures (Campisi et al., 2018, Hirschi and D'Amore, 1996, Kim et al., 2013), we investigated
368 the impact of pericytes on the resulting vascularized skin equivalents. HUVECs (10^7 cells/mL) were
369 seeded alone or together with human primary pericytes (10^6 cells/mL) in a 10 mg/mL fibrin within the
370 central channel of round chips. Side channels and the central well were supplemented with EGM-2

371 medium containing 50 ng/mL. After 4 days of culture to allow establishment of a mature
372 microvasculature, the dermal equivalent was introduced into the central well, followed by seeding of
373 N/TERT keratinocytes after 1 h, as previously described. Medium channels and the central well were
374 filled with FAD medium and culture was continued for 14 d, under submerged conditions
375 (Supplementary Figure S3). Cultures were fixed and dissected from chips for histological processing and
376 immunological staining. Sections taken from our samples were compared with *ex vivo* human skin
377 sections.

378 Resulting tissues displayed a well-structured multi-layer epidermal equivalent with flattened stratified
379 squamous cells (Figure 5 and Supplementary Figures S4 and S5). Although the overall thickness and
380 level of flattening and stratification of the epidermal compartment remained lower than what can be
381 observed in sections from human skin, epidermal equivalents were more developed in the presence of
382 microvasculatures (whether with or without pericytes). Rete ridges present in *in vivo* human skin were
383 also not observed in our HSE-chip models, although these are not generally recapitulated in other human
384 skin equivalent reported (Choudhury and Das, 2021). The overall depth of the epidermal compartment
385 significantly increased in vascularized chips (86 +/- 20.3 µm, for vascularized chips in the presence of
386 pericytes, compared to 64 +/- 26.5 µm, for avascular chips; Figure 5C). Although these thicknesses are
387 in line with those reported for skin equivalents (Chopra et al., 2015, Wei et al., 2017), our results indicate
388 that vascularization impacts on the establishment of the epidermal structure in skin equivalents.

389 To study this phenomenon further, we investigated stainings of tissue sections. The impact of
390 vascularization on the basal compartment of the epidermal equivalent was relatively modest. We
391 observed a small increase in the thickness of the basement membrane constituent laminin 332 in
392 vascularized chips, compared to avascular models and *ex vivo* skin sections (Figures 5B and E). This
393 increase was not statistically significant when comparing avascular and vascularized chips, but P values
394 decreased to <0.001 when pericyte/HUVEC vascular networks were used in the vascularised

395 compartment, compared to human skin sections. This modest change in basement membrane did not
396 translate into differences in expression of the basal marker keratin 14 (Figure 6). Similarly, Ki67 positive
397 cells in the epidermis were confined to the basal layer in all conditions and their frequency was
398 comparable (Figure 5D). However, these observations contrasted with the lack of Ki67 expression in the
399 basal compartment of *ex vivo* human skin sections, in line with previous observations made on
400 comparable human sections (Heenen et al., 1998).

401 Epidermal differentiation marker expression was more established and consistent with the addition of a
402 vascularized dermal compartment: the thickness of involucrin positive layers in chips containing either
403 HUVECs alone or alongside pericytes (8 +/- 5.8 and 8 +/- 3.8 µm, respectively) compared to avascular
404 models (3 +/- 2.2 µm, Figures A and D). However, involucrin expression remained weaker than in human
405 skin sections (10 +/- 2.9 µm). Similarly, staining for transglutaminase was significantly more pronounced
406 in vascularized, compared to avascular chips. Beyond expression levels, the localization of
407 transglutaminase was also more obviously localized at the upper layers of the epidermis in vascularized
408 HSE-chips, recapitulating well the pattern of expression typical of human skin sections (Figure 6B). We
409 did not observe a significant impact of vascularization on the thickness of transglutaminase expression
410 (Figure 6E), but expression was not confined to the uppermost layers of the epidermal equivalents in
411 avascular chips and could be seen in layers directly above the basal layer.

412 The impact of vascularization on the dermal compartment could also be clearly observed. CD31 positive
413 structures were obviously only observed in vascularized models, as would be expected from the presence
414 of endothelial cells (Figure 5B). Associated with such structures, we clearly observed an increase in
415 vimentin positive cells in vascularized chips, compared to avascular cultures (Figure 6B). Vimentin
416 positive cells were clearly denser in human skin histological sections, but this reflects a general higher
417 degree of cellularity in normal tissue dermis, compared to the in vitro models established.

418 Further characterization of the vascular compartment was carried out next. We observed extensive
419 dermal microvascular networks spanning the microfluidic compartments underlying the central well
420 cultures of chips loaded with HUVECs alone (bright field images, Figure 7), confirmed via staining for
421 the endothelial marker CD31 (Figure 7D). In the presence of pericytes, vascular networks were also
422 clearly observed, but displayed altered morphologies, in agreement with similar systems reported in the
423 literature (Kim et al., 2015b). Pericyte co-cultures displayed reduced total length and branching (Figures
424 7A-B). Such phenotype is proposed to be associated with the maturing and stabilizing role of pericytes,
425 enabling to better retain the stability of resulting networks. Mechanisms involved in this behavior remain
426 partially unclear, but may involve cytokine secretion (e.g. angiopoietin-1, angiogenin, HGF, TGF-a and
427 TNF) and perivascular matrix remodeling (Newman et al., 2011). Whilst others reported an impact on
428 endothelial cell-cell junctions (Jeon et al., 2014, Jeon et al., 2015), our previous results did not confirm
429 such effect.

430 To investigate the architecture of the microvasculatures integrated into the dermal equivalents in our
431 cultures, we examined the formation of capillaries in the sections generated (Figure 7D). CD31 and
432 laminin stainings clearly established the formation of rosettes associated with the formation of lumenated
433 capillaries (Figure 7D), in agreement with the recruitment of laminin at the basal membrane of micro-
434 capillaries (Black et al., 1998, Schurr et al., 1999, Kubota et al., 1988). The density of these structures
435 was clearly increased in HUVEC-pericytes co-cultures, indicating a better retention of the vascular
436 networks within these models (Figures 7C and D). The average external diameter of capillaries
437 determined from sections, although approximative as only relying on the ability to identify clear
438 transverse sections, were 12 +/- 6 µm for monocultures and 13 +/-6 µm for HUVEC/pericytes co-
439 cultures, which correspond to the external diameter of dermal arterial capillaries *in vivo*, identified from
440 human skin sections (Braverman, 2000). Overall, our results are evidencing the supportive role played

441 by pericytes in our model, maintaining the microvasculature integrity despite the use of mixed culture
442 media in our protocol (Campisi et al., 2018, Hirschi and D'Amore, 1996).

443 **4. Discussion**

444 Altogether these data demonstrate that our chip design enables the formation of a microvascular network
445 embedded in a multi-compartment microfluidic system and underlying the formation of a
446 dermal/epidermal skin. The design of a round central chamber and circumferential channels enables the
447 formation of a more homogenous microvasculature within the central compartment (Figure 2), in
448 agreement with previous data presented for a vascularized ocular model (Ko et al., 2019b). It is also
449 expected that the circular design selected will result in more homogenous cytokine and growth factor
450 gradients within the different compartments, as was previously described in a model of pluripotent stem
451 cell differentiation (Manfrin et al., 2019) and as briefly discussed in a model of central nervous system
452 axonal growth, across the diameter of a microfluidic compartment (Park et al., 2009).

453 A surprising result from our study is that skin equivalents, in the absence of microvasculature, form more
454 mature stratified epidermal compartments in submerged conditions, compared to those cultured at the
455 air-liquid interface. This contrasts with the literature indicating that culture at the air interface, for skin
456 equivalents grown in transwell systems, allows improved stratification and accurate epidermal
457 differentiation marker expression (Prunieras et al., 1983, Rosdy and Clauss, 1990). These results may be
458 explained by the smaller dimensions of the constructs generated and the lower volumes of media required
459 for their culture. Indeed, the smaller dimension may result in higher local oxygen concentrations,
460 impacting on keratinocyte commitment and stratification (Ngo et al., 2007). In addition, the smaller
461 volumes may allow greater accumulation of cytokines and growth factors promoting stratification. It may
462 also be that, the lower volumes of media used in culture at air-liquid interfaces in our chips result in
463 increased cell death, and that the added volume associated with submerged culture helps limiting such

464 process, as demonstrated by Lee et al. in 2017 in their vascularized skin-on-a-chip (Lee et al., 2017).
465 Indeed, tissues formed at the air-liquid interface displayed significantly reduced Ki67 expression,
466 compared to submerged systems (Figure 3).

467 Culture on microvascularized bed further improved the stratification and differentiation of skin
468 equivalents. The use of pericytes was found to have weak but statistically significant impacts on the
469 density of capillaries and their apparent lumenation in our skin equivalents (Figure 7). Therefore, beyond
470 their initial impact on the morphology of vascular networks, pericytes may contribute to the
471 complementarity of vascularized models with other tissue equivalents, allowing the formation of more
472 complex vascularized tissue models. This may be associated with perivascular matrix remodeling
473 (Avolio et al., 2017, Bergers and Song, 2005) and cytokine secretion, which were found to promote the
474 stability of vascular networks (Hurtado-Alvarado et al., 2014, Sounni et al., 2011).

475 Improved epidermal stratification and differentiation upon addition of a microvascular component has
476 previously been demonstrated in both *in vivo* mouse and *in vitro* systems (Baltazar et al., 2020).
477 Conversely, Rochon et al. have shown that various epithelial cell types have a direct impact on
478 endothelial vessel physiology *in vitro* (Rochon et al., 2009). This is likely due to increased bi-directional
479 diffusion of secreted growth factors and cytokines in the surrounding microenvironment, known to
480 impact differentiation in keratinocyte populations (Ansel et al., 1990, Gröne, 2002). Stromal fibroblasts
481 in the dermal equivalent matrix also likely contribute to the secreted factors to encourage improved
482 epidermal stratification; this has been demonstrated previously in human *in vitro* systems, which
483 commonly report an undifferentiated, unstratified epidermis' with a reduced thickness and poor
484 localization of upper-epidermal and basement membrane markers in the absence of proximal fibroblasts
485 (Saintigny et al., 1993). In 2020, Russo et al. published an extensive review on this topic (Russo et al.,
486 2020). Pericytes alongside HUVECs have been shown to increase epidermal thickness and the expression
487 of cytokeratins 1/10 and laminin 332 in *in vitro* skin models, which was also confirmed in engraftment

488 experiments into a murine setting for a duration of 4 weeks (Baltazar et al., 2020). In agreement with this
489 literature, stromal cell interactions are proposed to improve epidermal architecture in our model.

490 Overall, our results demonstrate the feasibility of hierarchically structured vascularized-skin-on-chip
491 equivalents, paving the way for the embedding of these systems for testing of therapeutics safety and
492 efficacy testing in a human context in vitro. Such models will allow testing of systemic as well as topical
493 delivery in realistic scenarios, in platforms that may be compatible with high throughput testing. This
494 still requires the engineering of multi-chip plate systems compatible with high throughput formats, in
495 analogy to some of the epithelial/endothelial tissue models developed on the Emulate platforms (Si et
496 al., 2021), and the parallelization of multi-cellular culture and embedding in the resulting micro-
497 engineered chips. This latter process may require particular attention from the research community as
498 parallelized and automated multi-cell culture systems have not been engineered to date.

499 **3 Conflict of Interest**

500 The authors declare that the research was conducted in the absence of any commercial or financial
501 relationships that could be construed as a potential conflict of interest.

502 **4 Author Contributions**

503 CFEJ, JEG and JC: conceptualization and project administration. CFEJ: data curation, formal analysis,
504 and validation, visualization and writing – original draft. JEG and JC: funding acquisition, resources and
505 supervision. SC: data curation. JEG: writing – review and editing. All authors contributed to the article
506 and approved the submitted version.

507 **5 Funding**

508 This work was funded by the Engineering and Physical Sciences Research Council of UK Research and
509 Innovation (EPSRC grant EP/N50953X/1).

6 Acknowledgments

The authors would like to acknowledge the contribution of Atiya Sarmin (Blizard Institute, Whitechapel) for helping to formulate the dermal equivalent employed in our model.

7 Supplementary Material

Supplementary immunostainings of vascularised chips and histology sections are available as supplementary information or from the authors.

8 Data Availability Statement

The raw data supporting the conclusions of this article will be made available by the authors, without undue reservation.

9 References

Ackermann, K., Lombardi Borgia, S., Korting, H. C., Mewes, K. R. & Schäfer-Korting, M. 2010. The Phenion® Full-Thickness Skin Model for Percutaneous Absorption Testing. *Skin Pharmacology and Physiology,* 23**,** 105-112.

Ansel, J., Perry, P., Brown, J., Damm, D., Phan, T., Hart, C., Luger, T. & Hefeneider, S. 1990. Cytokine modulation of keratinocyte cytokines. *Journal of Investigative Dermatology,* 94**,** s101-107.

Asbill, C., Kim, N., El-Kattan, A., Creek, K., Wertz, P. & Michniak, B. 2000. Evaluation of a human bio-engineered skin equivalent for drug permeation studies. *Pharm. Res.,* 17**,** 1092-1097.

Avolio, E., Alvino, V. V., Ghorbel, M. T. & Campagnolo, P. 2017. Perivascular cells and tissue engineering: current applications and untapped potential. *Pharmcology & Therapeutics,* 171**,** 83-92.

531 Baish, J. W., Stylianopoulos, T., Lanning, R. M., Kamoun, W. S., Fukumura, D., Munn, L. L. & Jain,
532 R. K. 2011. Scaling rules for diffusive drug delivery in tumor and normal tissues. *Proc. Natl.*
533 *Acad. Sci.,* 108**,** 1799-1803.

534 Baltazar, T., Merola, J., Catarino, C., Xie, C. B., Kirkiles-Smith, N. C., Lee, V., Hotta, S., Dai, G., Xu,
535 X., Ferreira, F. C., Saltzman, W. M., Pober, J. S. & Karande, P. 2020. Three Dimensional
536 Bioprinting of a Vascularized and Perfusable Skin Graft Using Human Keratinocytes,
537 Fibroblasts, Pericytes, and Endothelial Cells. *Tissue Engineering, Part A,* 26**,** 227-238.

538 Bellas, E., Seiberg, M., Garlick, J. & Kaplan, D. L. 2012. In vitro 3D full-thickness skin-equivalent
539 tissue model using silk and collagen biomaterials. *Macromol. Biosci.,* 12**,** 1627-1636.

540 Bergers, G. & Song, S. 2005. The role of pericytes in blood-vessel formation and maintenance. *Neuro-*
541 *Oncology,* 7**,** 452-464.

542 Black, A. F., Berthod, F., L'heureux, N., Germain, L. & Auger, F. A. 1998. In vitro reconstruction of a
543 human capillary-like network in a tissue-engineered skin equivalent. *Faseb J,* 12**,** 1331-1340.

544 Bosch-Fortea, M., Rodriguez-Fraticelli, A. E., Herranz, G., Hachimi, M., Barea, M. D., Young, J.,
545 Ladoux, B. & Martin-Belmonte, F. 2019. Micropattern-based platform as a physiologically
546 relevant model to study epithelial morphogenesis and nephrotoxicity. *Biomaterials,* 218**,**
547 119339.

548 Braverman, I. M. 2000. The cutaneous microcirculation. *J Investig. Dermatol. Symp. Proc.,* 5**,** 3-9.

549 Campisi, M., Shin, Y., Osaki, T., Hajal, C., Chiono, V. & Kamm, R. D. 2018. 3D self-organized
550 microvascular model of the human blood-brain barrier with endothelial cells, pericytes and
551 astrocytes. *Biomaterials,* 180**,** 117-129.

552 Chen, C. S., Mrksich, M., Huang, S., Whitesides, G. M. & Ingber, D. E. 1997. Geometric control of
553 cell life and death. *Science,* 276**,** 1425-1428.

554 Chen, M. B., Whisler, J. A., Frose, J., Yu, C., Shin, Y. & Kamm, R. D. 2017. On-chip human
555 microvasculature assay for visualization and quantification of tumor cell extravasation
556 dynamics. *Nat. Protoc.,* 12**,** 865-880.

557 Chopra, K., Calva, D., Sosin, M., Tadisina, K. K., Banda, A., De La Cruz, C., Chaudhry, M. R.,
558 Legesse, T., Drachenberg, C. B., Manson, P. N. & Christy, M. R. 2015. A comprehensive
559 examination of topographic thickness of skin in the human face. *Aesthetic Surgery Journal,* 35**,**
560 1007-1013.

561 Choudhury, S. & Das, A. 2021. Advances in generation of three-dimensional skin equivalents: pre-
562 clinical studies to clinical therapies. *Cytotherapy,* 23**,** 1-9.

563 Coloma, M. J., Morrison, S. L., Helmlinger, G., Yuan, F., Dellian, M. & Jain, R. K. 1997. Interstitial
564 pH and pO 2 gradients in solid tumors in vivo: high-resolution measurements reveal a lack of
565 correlation. *Nat. Med.,* 3**,** 177-182.

566 Colton, C. K. 1995. Implantable biohybrid artificial organs. *Cell Transplantation,* 4**,** 415-436.

567 Commandeur, S., Van Drongelen, V., De Gruijl, F. R. & El Ghalbzouri, A. 2012. Epidermal growth
568 factor receptor activation and inhibition in 3D in vitro models of normal skin and human
569 cutaneous squamous cell carcinoma. *Cancer Sci.,* 103**,** 2120-2126.

570 Connelly, J., Gautrot, J. E., Trappmann, B., Tan, D. W. M., Donati, G., Huck, W. T. S. & Watt, F. M.
571 2010. Actin and SRF transduce physical cues from the microenvironment to regulate epidermal
572 stem cell fate decisions. *Nat. Cell Biol.,* 12**,** 711-718.

573 Costa, P., Gautrot, J. E. & Connelly, J. 2014. Directing cell migration using micropatterned and
574 dynamically adhesive polymer brushes. *Acta Biomater,* 10**,** 2415-2422.

575 Enjalbert, F., Priya Dewan, P., Caley, M. P., Jones, E. M., Morse, M. A., Kelsell, D. P., Enright, A. J.
576 & O'toole, E. A. 2020. 3D model of harlequin ichthyosis reveals inflammatory therapeutic
577 targets. *J Clin. Invest.,* 130**,** 4798-4810.

578 Galie, P. A., Nguyen, D.-H. T., Choi, C. K., Cohen, D. M., Janmey, P. A. & Chen, C. S. 2014. Fluid
579 shear stress threshold regulates angiogenic sprouting. *Proc. Natl. Acad. Sci.,* 111**,** 7968-7973.

580 Gautrot, J. E., Wang, C., Liu, X., Goldie, S. J., Trappmann, B., Huck, W. T. S. & Watt, F. M. *2012*.
581 Mimicking normal tissue architecture and perturbation in cancer with engineered micro-
582 epidermis. *Biomaterials,* 33**,** 5221-5229.

583 Gröne, A. 2002. Keratinocytes and cytokines. *Veterinary Immunology and Immunopathology,* 88**,** 1-12.

584 Hassell, B. A., Goyal, G., Lee, E. J., Sontheimer-Phelps, A., Levy, O., Chen, C. S. & Ingber, D. E.
585 2017. Human organ chip models recapitulate orthotopic lung cancer growth, therapeutic
586 responses, and tumour dormancy in vitro. *Cell Reports,* 21**,** 508-516.

587 Heenen, M., Thiriar, S., Noël, J. C. & Galand, P. 1998. Ki-67 immunostaining of normal human
588 epidermis: Comparison with 3H-thymidine labelling and PCNA immunostaining. *Dermatology,*
589 197**,** 123-126.

590 Hernández Vera, R., Genové, E., Alvarez, L., Borrós, S., Kamm, R., Lauffenburger, D. & Semino, C.
591 E. 2008. Interstitial fluid flow intensity modulates endothelial sprouting in restricted Src-
592 activated cell clusters during capillary morphogenesis. *Tissue Engineering Part A,* 15**,** 175-185.

593 Hirschi, K. K. & D'amore, P. A. 1996. Pericytes in the microvasculature. *Cardiovascular Res.,* 32**,**
594 687-698.

595 Homan, K. A., Gupta, N., Kroll, K. T., Kolesky, D. B., Skylar-Scott, M., Miyoshi, T., Mau, D.,
596 Valerius, M. T., Ferrante, T., Bonventre, J. V., Lewis, J. A. & Morizane, R. 2019. Flow-

597 enhanced vascularization and maturation of kidney organoids in vitro. *Nat. Methods,* 16**,** 255-
598 262.

599 Huh, D., Matthews, B. D., Mammoto, A., Montoya-Zavala, M., Hsin, H. Y. & Ingber, D. E. 2010.
600 Reconstituting organ-level lung function on a chip. *Science,* 328**,** 1662-1668.

601 Hurtado-Alvarado, G., Cabañas-Morales, A. M. & Gómez-Gónzalez, B. 2014. Pericytes: brain-immune
602 interface modulators. *Frontiers in Integrative Neuroscience,* 7**,** 80.

603 Jenkins, G. 2013. Rapid prototyping of PDMS devices using SU-8 lithography. *Microfluidic*
604 *Diagnostics: Methods and Protocols,* 949**,** 153-168.

605 Jeon, J. S., Bersini, S., Gilardi, M., Dubini, G., Charest, J. L., Moretti, M. & Kamm, R. D. 2015.
606 Human 3D vascularized organotypic microfluidic assays to study breast cancer cell
607 extravasation. *Proc. Natl. Acad. Sci.,* 112**,** 214-219.

608 Jeon, J. S., Bersini, S., Whisler, J. A., Chen, M. B., Dubini, G., Charest, J. L., Moretti, M. & Kamm, R.
609 D. 2014. Generation of 3D functional microvascular networks with human mesenchymal stem
610 cells in microfluidic systems. *Integr. Biol.,* 6**,** 555-563.

611 Kilic, O., Pamies, D., Lavell, E., Schiapparelli, P., Feng, Y., Hartung, T., Bal-Price, A., Hogberg, H. T.,
612 Quinones-Hinojosa, A., Guerrero-Cazares, H. & Levchenko, A. 2016. Brain-on-a-chip model
613 enables analysis of human neuronal differentiation and chemotaxis. *Lab Chip,* 16**,** 4152-4162.

614 Kim, B. S., Gao, G., Kim, J. Y. & Cho, D. W. 2019. 3D Cell Printing of Perfusable Vascularized
615 Human Skin Equivalent Composed of Epidermis, Dermis, and Hypodermis for Better Structural
616 Recapitulation of Native Skin. *Adv. Healthcare Mater.,* 8**,** 1-11.

617 Kim, C., Kasuya, J., Jeon, J., Chung, S. & Kamm, R. D. 2015a. A quantitative microfluidic
618 angiogenesis screen for studying anti-angiogenic therapeutic drugs. *Lab Chip,* 15**,** 301-310.

619 Kim, H. J. & Ingber, D. E. 2013. Gut-on-a-chip microenvironment induces human intestinal cells to
620 undergo villus differentiation. *Integr. Biol.,* 5**,** 1130-1140.

621 Kim, J., Chung, M., Kim, S., Jo, D. H., Kim, J. H. & Jeon, N. L. 2015b. Engineering of a Biomimetic
622 Pericyte-Covered 3D Microvascular Network. *PLoS One,* 10**,** e0133880.

623 Kim, S., Chung, M., Ahn, J., Lee, S. & Jeon, N. L. 2016. Interstitial flow regulates the angiogenic
624 response and phenotype of endothelial cells in a 3D culture model. *Lab Chip,* 16**,** 4189-4199.

625 Kim, S., Lee, H., Chung, M. & Jeon, N. L. 2013. Engineering of functional perfusable 3D
626 microvascular networks on a chip. *Lab Chip,* 13**,** 1489-1500.

627 Ko, J., Ahn, J., Kim, S., Lee, Y., Lee, J., Park, D. & Jeon, N. L. 2019a. Tumor spheroid-on-a-chip: a
628 standardized microfluidic culture platform for investigating tumor angiogenesis. *Lab Chip,* 19**,**
629 2822-2833.

630 Ko, J., Lee, Y., Lee, S., Lee, S. R. & Jeon, N. L. 2019b. Human Ocular Angiogenesis-Inspired
631 Vascular Models on an Injection-Molded Microfluidic Chip. *Adv. Healthcare Mater.,* 8**,** 1-10.

632 Kubota, Y., Kleinman, H. K., Martin, G. R. & Lawley, T. J. 1988. Role of laminin and basement
633 membrane in the morphological differentiation of human endothelial cells into capillary-like
634 structures. *J. Cell Biol.,* 107**,** 1589-1598.

635 Kwak, B. S., Jin, P., Kim, S. J., Kim, E. J., Chung, J. H. & Sung, J. H. 2020. Microfluidic skin chip
636 with vasculature for recapitulating the immune response of the skin tissue. *Biotech. Bioeng.,*
637 117**,** 1853-1863.

638 Lancaster, M. A., Renner, M., Martin, C.-A., Wenzel, D., Bicknell, L. S., Hurles, M. E., Homfray, T.,
639 Penninger, J. M., Jackson, A. P. & Knoblich, J. A. 2013. Cerebral organoids model human
640 brain development and microcephaly. *Nature,* 501**,** 373-379.

641 Langan, E. A., Philpott, M. P., Kloepper, J. E. & Paus, R. 2015. Human air follicle organ culture:
642 theory, application and perspectives. *Experimental Dermatology,* 24**,** 903-911.

643 Lee, J., Rabbani, C. C., Gao, H., Steinhart, M. R., Woodruff, B. M., Pflum, Z. E., Kim, A., Heller, S.,
644 Liu, Y., Shipchandler, T. Z. & Koehler, K. R. 2020. Hair-bearing human skin generated entirely
645 from pluripotent stem cells. *Nature,* 582**,** 399-404.

646 Lee, S., Jin, S.-P. P., Kim, Y. K., Sung, G. Y., Chung, J. H. & Sung, J. H. 2017. Construction of 3D
647 multicellular microfluidic chip for an in vitro skin model. *Biomed Microdevices,* 19**,** 22.

648 Li, L., Fukunaga-Kalabis, M. & Herlyn, M. 2011. The Three-Dimensional Human Skin Reconstruct
649 Model: a Tool to Study Normal Skin and Melanoma Progression. *Journal of Visualized*
650 *Experiments,* 12**,** 1-5.

651 Liu, J. F., Long, H. Y., Zeuschner, D., Rader, A. F. B., Polacheck, W. J., Kessler, H., Sorokin, L. &
652 Trappmann, B. 2021. Synthetic extracellular matrices with tailored adhesiveness and
653 degradability support lumen formation during angiogenic sprouting. *Nat. Commun.,* 12**,** 3402.

654 Liu, Y., Suwa, F., Wang, X., Takemura, A., Fang, Y. R., Li, Y., Zhao, Y. & Jin, Y. 2007.
655 Reconstruction of a tissue-engineered skin containing melanocytes. *Cell Biology International,*
656 31**,** 985-990.

657 Loskill, P., Hardwick, R. N. & Roth, A. 2021. Challenging the pipeline. *Stem Cell Rep.,* 16**,** 2033-2043.

658 Manfrin, A., Tabata, Y., Paquet, E. R., Vuaridel, A. R., Rivest, F. R., Naef, F. & Lutolf, M. P. 2019.
659 Engineered signaling centers for the spatially controlled patterning of human pluripotent stem
660 cells. *Nat. Methods,* 16**,** 640-648.

661 Mazlyzam, A. L., Aminuddin, B. S., Fuzina, N. H., Norhayati, M. M., Fauziah, O., Isa, M. R., Saim, L.
662 & Ruszymah, B. H. I. 2007. Reconstruction of living bilayer human skin equivalent utilizing
663 human fibrin as a scaffold. *Burns,* 33**,** 355-363.

664 Menon, N. V., Tay, H. M., Wee, S. N., Li, K. H. H. & Hou, H. W. 2017. Micro-engineered perfusable
665 3D vasculatures for cardiovascular diseases. *Lab Chip,* 17**,** 2960-2968.

666 Nelson, C. M., Vanduijn, M. M., Inman, J. L., Fletcher, D. A. & Bissell, M. J. 2006. Tissue Geometry
667 Determines Sites of Mammary Branching Morphogenesis in Organotypic Cultures. *Science,*
668 314**,** 298-300.

669 Newman, A. C., Nakatsu, M. N., Chou, W., Gershon, P. D. & Hughes, C. C. W. 2011. The requirement
670 for fibroblasts in angiogenesis: fibroblast-derived matrix proteins are essential for endothelial
671 cell lumen formation. *Molec. Biol. Cell,* 22**,** 3791-3800.

672 Ngo, M. A., Sinitsyna, N. N., Qin, Q. & Rice, R. H. 2007. Oxygen-dependent differentiation of human
673 keratinocytes. *J. Invest. Dermatol.,* 127**,** 354-361.

674 Park, J., Koito, H., Li, J. & Han, A. 2009. Microfluidic compartmentalized co-culture platform for CNS
675 axon myelination research. *Biomed. Microdevices,* 11**,** 1145-1153.

676 Polacheck, W. J., German, A. E., Mammoto, A., Ingber, D. E. & Kamm, R. D. 2014.
677 Mechanotransduction of fluid stresses governs 3D cell migration. *Proc. Natl. Acad. Sci.,* 111**,**
678 2447-2452.

679 Prunieras, M., Regnier, M. & Woodley, D. 1983. Methods of cultivation of keratinocytes with an air-
680 liquid interface. *J. Invest. Dermatol.,* 81**,** 28s-33s.

681 Rochon, M.-H., Fradette, J., Fortin, V., Tomasetig, F., Roberge, C. J., Baker, K., Berthod, F., Auger, F.
682 & Germain, L. 2009. Normal Human Epithelial Cells Regulate the Size and Morphology of
683 Tissue-Engineered Capillaries. *Tissue Engineering,* 16**,** 1457-1469.

684 Ronaldson-Bouchard, K., Ma, S. P., Yeager, K., Chen, T., Song, L. J., Sirabella, D., Morikawa, K.,
685 Teles, D., Yazawa, M. & Vunjak-Novakovic, G. 2018. Advanced maturation of human cardiac
686 tissue grown from pluripotent stem cells. *Nature,* 556**,** 239-243.

687 Rosdy, M. & Clauss, L. C. 1990. Terminal epidermal differentiation of human keratinocytes grown in
688 chemically defined medium on inert filter substrates at the air-liquid interface. *J. Invest.*
689 *Dermatol.,* 95**,** 409-414.

690 Ruiz, S. A. & Chen, C. S. 2008. Emergence of patterned stem cell differentiation within multicellular
691 structures. *Stem Cells,* 26**,** 2921-2927.

692 Russo, B., Brembilla, N. C. & Chizzolini, C. 2020. Interplay between keratinocytes and fibroblasts: A
693 systematic review providing a new angle for understanding skin fibrotic disorders. *Frontiers*
694 *Immunology,* 11**,** 648.

695 Saintigny, G., Bonnard, M., Damour, O. & Collombel, C. 1993. Reconstruction of epidermis on a
696 chitosan cross-linked collagen-GAG lattice: effect of fibroblasts. *Acta Dermato-Venereologica,*
697 73**,** 175-180.

698 Sakar, M. S., Eyckmans, J., Pieters, R., Eberli, D., Nelson, B. J. & Chen, C. S. 2016. Cellular forces
699 and matrix assembly coordinate fibrous tissue repair. *Nat. Commun.,* 7**,** 11036.

700 Schurr, M. J., Foster, K. N., Centanni, J. M., Comer, A. R., Wicks, A., Gibson, A. L., Thomas-Virnig,
701 C. L., Schlosser, J., Faucher, L. D., Lokuta, M. A., Allen-Hoffmann, B. L., Black, A. F., Hudon,
702 V., Damour, O., Germain, L. & Auger, F. A. 1999. A novel approach for studying angiogenesis:
703 a human skin equivalent with a capillary-like network. *Cell Biol. Toxicology,* 15**,** 81-90.

704 Shahabeddin, L., Berthod, F., Damour, O. & Collombel, C. 1990. Characterization of Skin
705 Reconstructed on a Chitosan-Cross-Linked Collagen-Glycosaminoglycan Matrix. *Skin*
706 *Pharmacology and Physiology,* 3**,** 107-114.

707 Shin, N., Kim, Y., Ko, J., Choi, S. W., Hyung, S., Lee, S., Park, S., Song, J., Jeon, N. L. & Kang, K.
708 2021. Vascularization of iNSC spheroid in a 3D spheroid-on-a-chip platform enhances neural
709 maturation. *Biotechnology and Bioengineering,* 119**,** 566-574.

710 Si, L., Bai, H., Rodas, M., Cao, W., Oh, C. Y., Jiang, A., Moller, R., Hoagland, D., Oishi, K., Horiuchi,
711 S., Uhl, S., Blanco-Melo, D., Albrecht, R. A., Liu, W. C., Jordan, T., Nilsson-Payant, B. E.,
712 Golynker, I., Frere, J., Logue, J. & Ingber, D. E. 2021. A human-airway-on-a-chip for the rapid
713 identification of candidate antiviral therapeutics and prophylactics. *Nat. Biomed. Eng.,* 5**,** 815-
714 829.

715 Sobrino, A., Phan, D. T. T., Datta, R., Wang, X., Hachey, S. J., Romero-Lopez, M., Gratton, E., Lee,
716 A. P., George, S. C. & Hughes, C. C. W. 2016. 3D microtumors in vitro supported by perfused
717 vascular networks. *Scientific Reports,* 6**,** 31589.

718 Sounni, N. E., Paye, A., Host, L. & Noël, A. 2011. MT-MMPS as regulators of vessel stability
719 associated with angiogenesis. *Frontiers in Pharmacology,* 2**,** 111.

720 Stark, H. J., Boehnke, K., Mirancea, N., Willhauck, M. J., Pavesio, A., Fusenig, N. E. & Boukamp, P.
721 2006. Epidermal homeostasis in long-term scaffold-enforced skin equivalents. *J Investig*
722 *Dermatol Symp Proc,* 11**,** 93-105.

723 Stephens, P., Grenard, P., Aeschlimann, P., Langley, M., Blain, E., Errington, R., Kipling, D., Thomas,
724 D. & Aeschlimann, D. 2004. Crosslinking and G-protein functions of transglutaminase 2
725 contribute differentially to fibroblast wound healing responses. *J Cell Sci,* 117**,** 3389-3403.

726 Tan, K. Y., Lin, H., Madeleine, R., Watt, F. M., Huck, W. T. S. & Gautrot, J. E. 2013. Decoupling
727 geometrical and chemical cues directing epidermal stem cell fate on polymer brush-based cell
728 micro-patterns. *Integrative Biology,* 5**,** 899-910.

729 Trappmann, B., Baker, B. M., Polacheck, W. J., Choi, C. K., Burdick, J. A. & Chen, C. S. 2017. Matrix
730 degradability controls multicellularity of 3D cell migration. *Nat. Commun.,* 8**,** 371.

731 Watt, F. M., Jordan, P. W. & O'neill, C. H. 1988. Cell shape controls terminal differentiation of human
732 epidermal keratinocytes. *Proc. Natl. Acad. Sci.,* 85**,** 5576-5580.

733 Wei, J. C. J., Edwards, G. A., Martin, D. J., Huang, H., Crichton, M. L. & Kendall, M. a. F. 2017.
734 Allometric scaling of skin thickness, elasticity, viscoelasticity to mass for micro-medical device
735 translation: From mice, rats, rabbits, pigs to humans. *Scientific Reports,* 7**,** 15885.

736 Wufuer, M., Lee, G. H., Hur, W., Jeon, B., Kim, B. J., Choi, T. H. & Lee, S. H. 2016. Skin-on-a-chip
737 model simulating inflammation, edema and drug-based treatment. *Scientific Reports,* 6**,** 37471.

738

739

Design of an Integrated Microvascularised Human Skin-on-a-Chip Tissue Equivalent Model

Figures

Christian F. E. Jones[1,2], Stefania di Ciò[1,2], John Connelly[3], Julien Gautrot[1,2*]

[1]Institute of Bioengineering and [2]School of Engineering and Materials Science, Queen Mary University of London, London, United Kingdom

[3]The Blizard Institute, Queen Mary University of London, London, United Kingdom

*** Correspondence:**
Julien Gautrot
j.gautrot@qmul.ac.uk

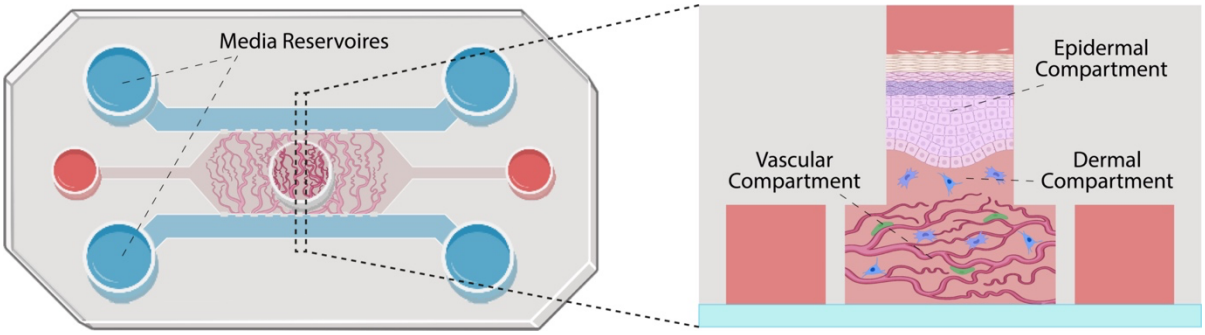

Figure 1. Schematic representation of the skin-on-a-chip model proposed. The chip is constituted of three parallel channels separated by microposts and connecting media reservoirs. A central well is positioned in the centre of the central channel. The vascular compartment is formed in the central channel (microvasculature shown in red and pericytes in green). Dermal fibroblasts (in blue) are introduced within a second hydrogel compartment, in the central well, before keratinocytes are seeded and allowed to stratify (in pink).

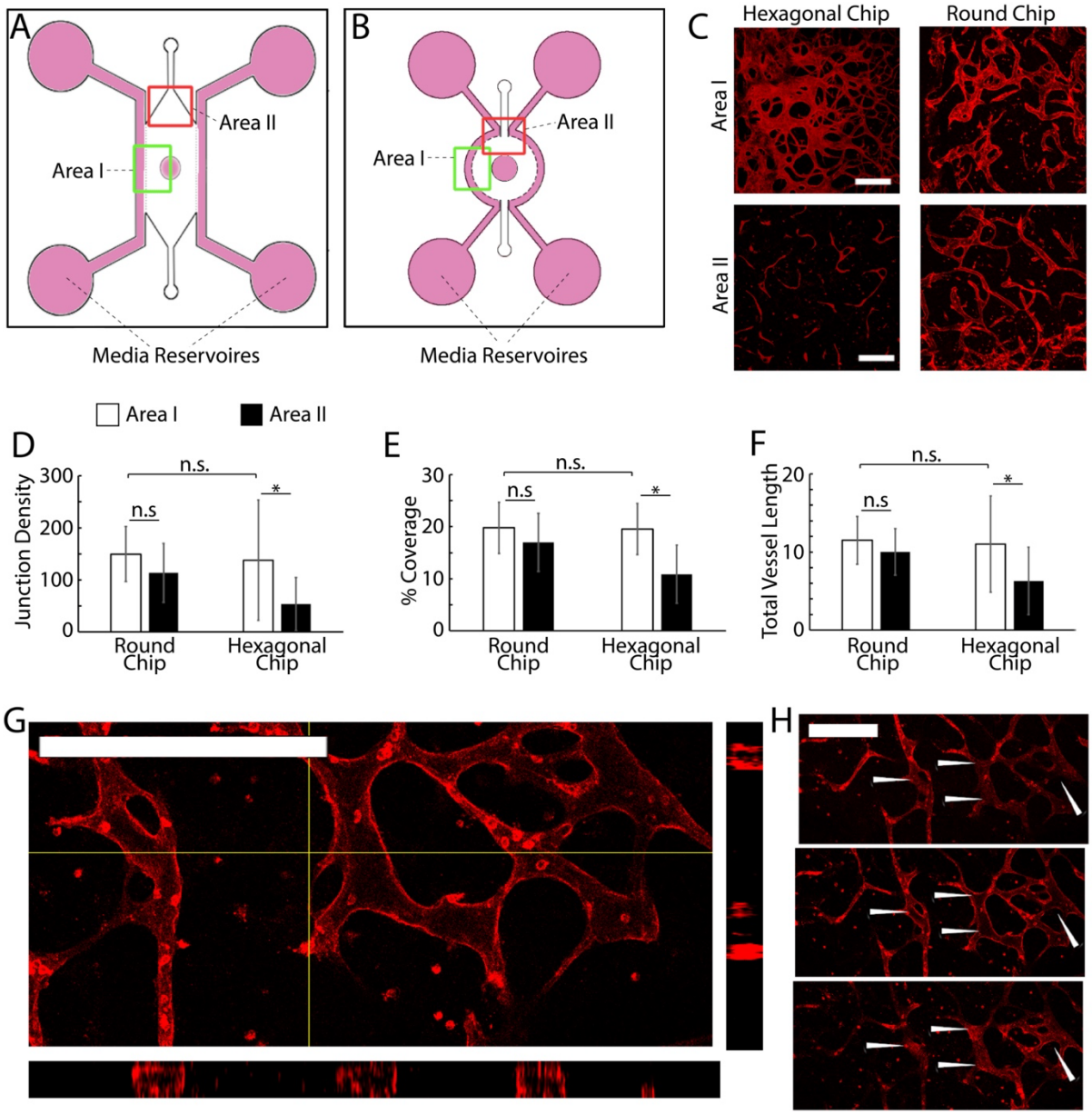

Figure 2. A, B) Schematic representation of the two chip designs investigated. C) Examples of microvascular networks formed in different areas of the central compartment of hexagonal and round chips. D-F) Quantification of the morphology of corresponding networks. G-H) Confocal images of networks formed in round chips displaying lumenated structures (G, z-stack projection and cross-section; H, corresponding individual sections taken across one network branch). *$P < 0.05$; n.s., non significant, $P > 0.05$; error bars are standard errors; n=3.

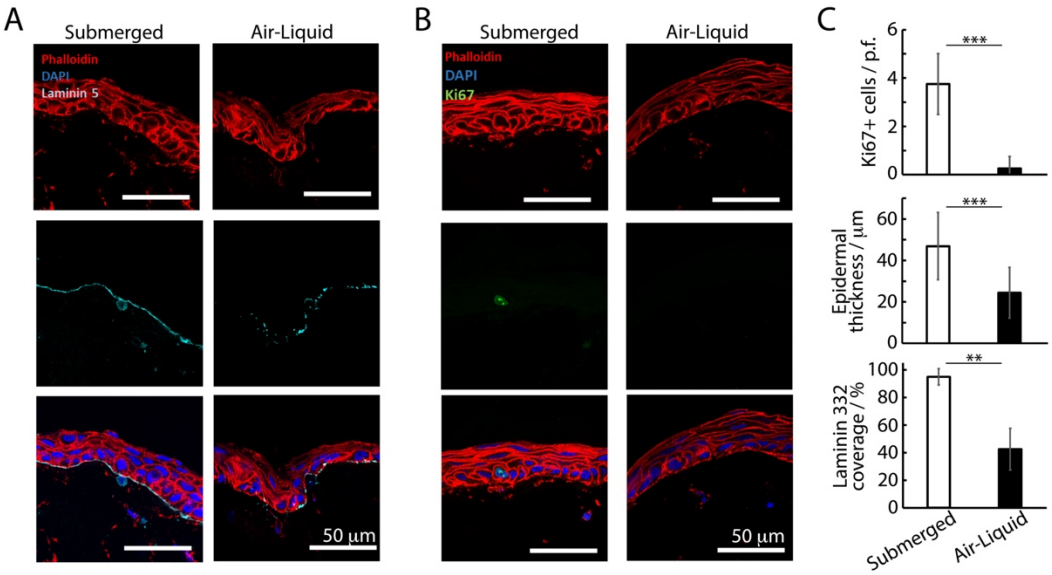

Figure 3. Histology sections of avascular skin-on-chip constructs immuno-stained with phalloidin (red), DAPI (blue) and for laminin 332 (A, cyan) or Ki67 (B, green). After an initial culture of 7 days, tissues were further cultured for 7 days in submerged or air-liquid conditions. C) Quantification of the corresponding density of Ki67+ cells, epidermal thickness and coverage of laminin 332. **P < 0.01; ***P < 0.001; n.s., non significant, P > 0.05; error bars are standard errors; n=3.

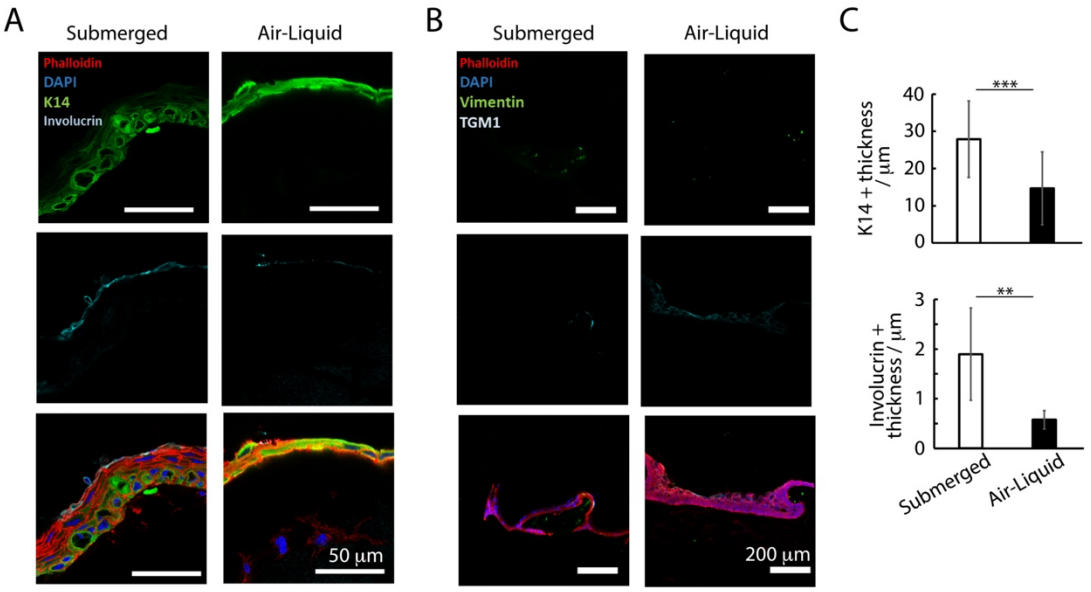

Figure 4. Histology sections of avascular skin-on-chip constructs immuno-stained with phalloidin (red), DAPI (blue), and for K14 and involucrin (green and cyan, respectively; A), or for vimentin and transglutaminase (green and cyan, respectively, B). After an initial culture of 7 days, tissues were further cultured for 7 days in submerged or air-liquid conditions. C) Quantification of the corresponding density of K14+ tissue thickness and involucrin positive tissue thickness. **P < 0.01; ***P < 0.001; n.s., non significant, P > 0.05; error bars are standard errors; n=3.

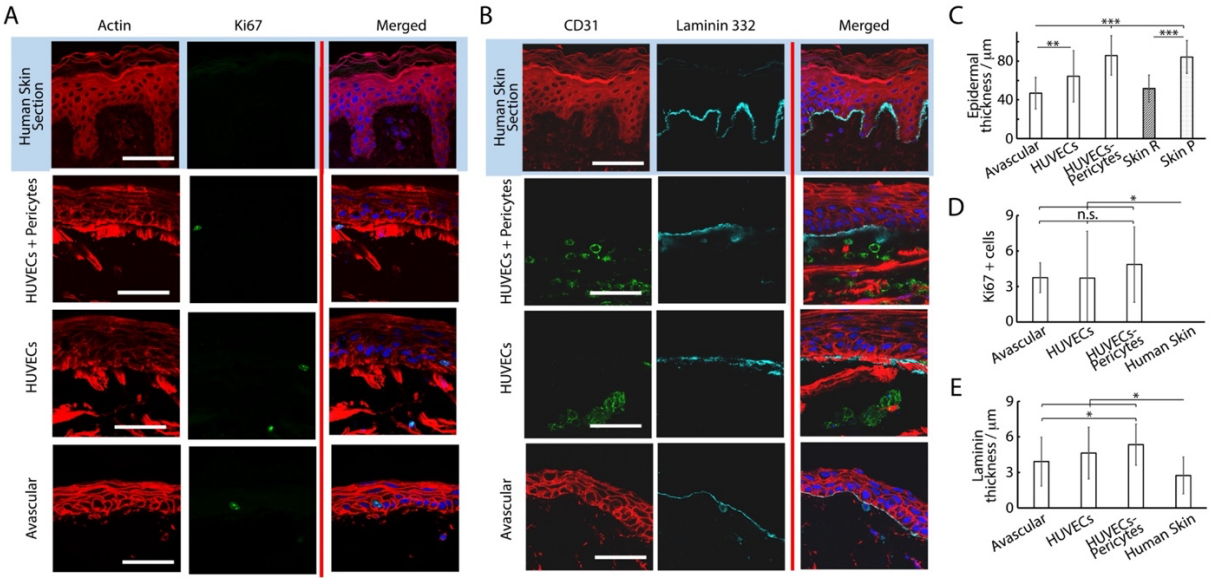

Figure 5. Histology sections of microvascularised skin-on-chip constructs and human skin sections immuno-stained with phalloidin (red), DAPI (blue) and for Ki67 (A, green) or CD31 and laminin 332 (B, green and cyan, respectively). Tissues were cultured for 14 days in submerged conditions. C) Quantification of the corresponding epidermal thickness (C), density of Ki67+ cells (D) and thickness of laminin 332 (E). *P < 0.05; **P < 0.01; ***P < 0.001; n.s., non significant, P > 0.05; error bars are standard errors; n=3.

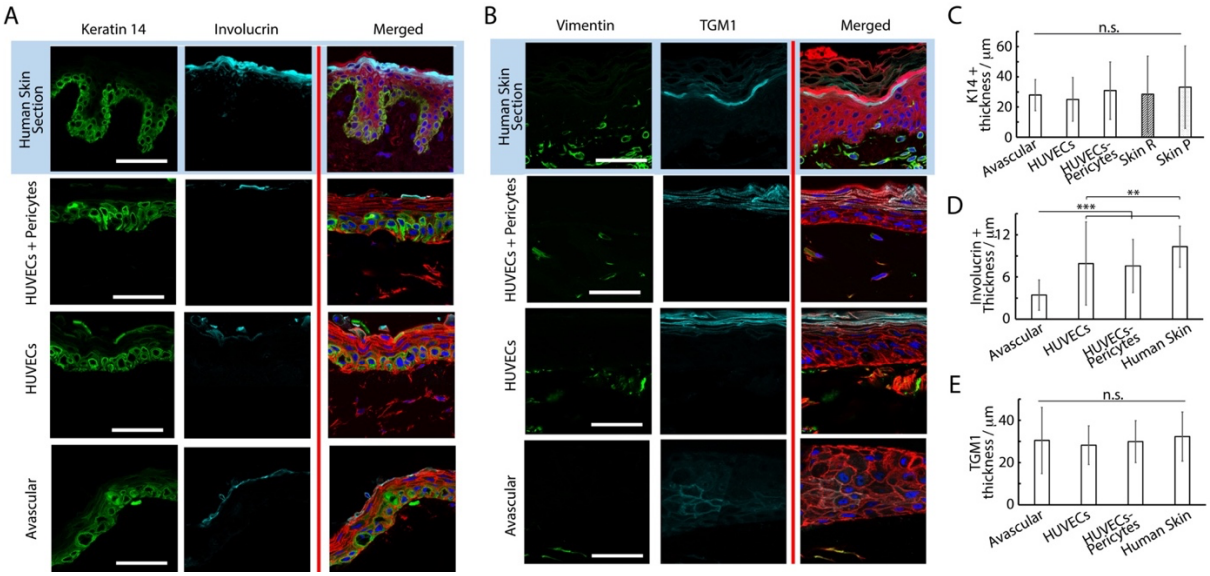

Figure 6. Histology sections of microvascularised skin-on-chip constructs and human skin sections immuno-stained with phalloidin (red), DAPI (blue) and for K14 and involucrin (A, green and cyan, respectively) or vimentin and transglutaminase (B, green and cyan, respectively). Tissues were cultured for 14 days in submerged conditions. C) Quantification of the corresponding K14+ tissue thickness (C), involucrin + tissue thickness (D) and transglutaminase + tissue thickness (E). **P < 0.01; ***P < 0.001; n.s., non significant, P > 0.05; error bars are standard errors; n=3.

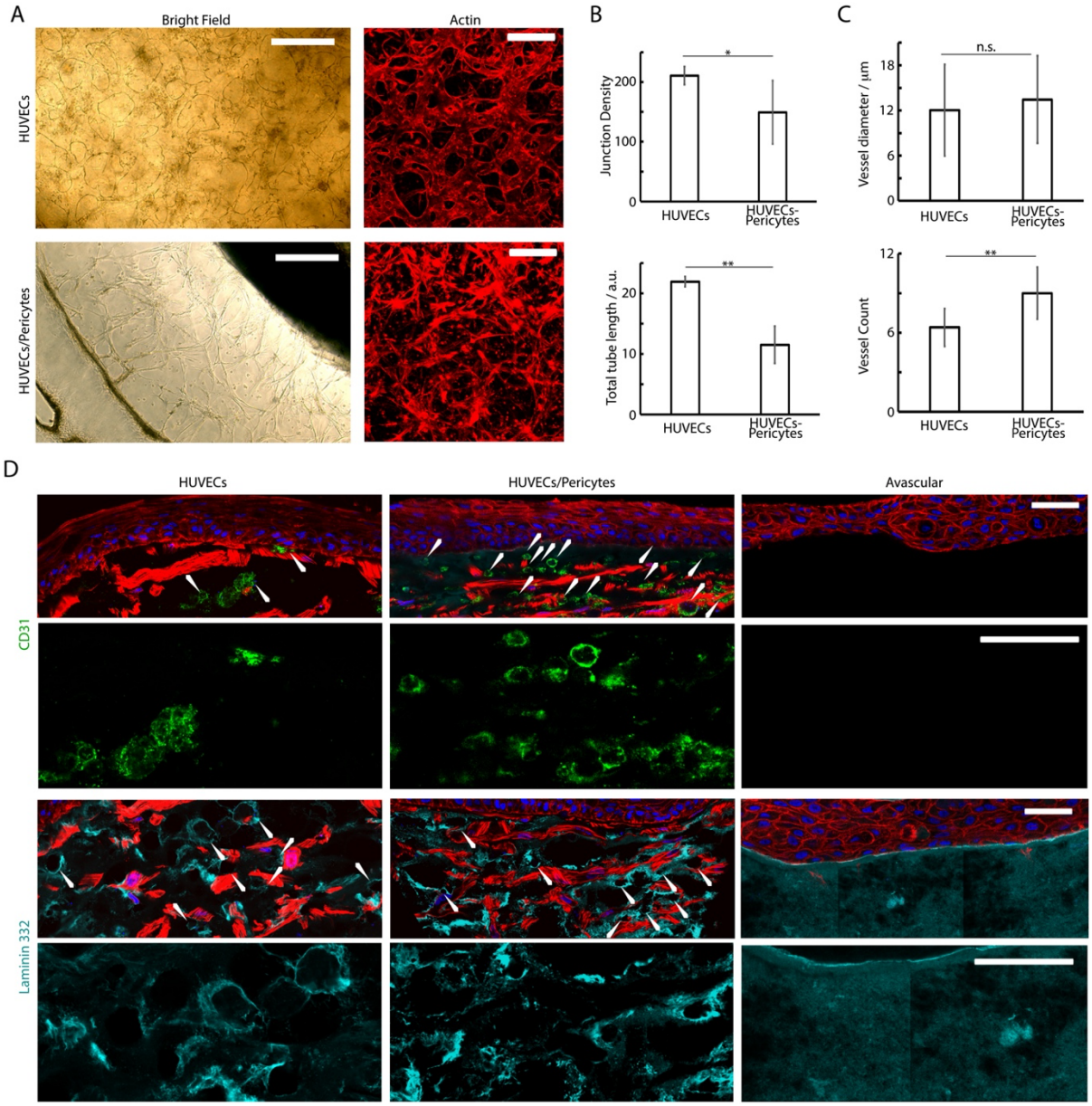

Figure 7. A) Brightfield and confocal images (phalloidin) of the basal microvascular compartment of chips injected with either HUVECs alone or HUVEC and pericytes, followed by 4 days of culture in EGM2 medium + 50 ng/mL VEGF and 2 weeks in FAD medium. B and C) Characterisation of the morphology of the corresponding networks. D) Histology sections of microvascularised skin-on-chip constructs immuno-stained with phalloidin (red), DAPI (blue), and for CD31 (green) and laminin 332 (cyan). Tissues were cultured for 14 days in submerged conditions. *$P < 0.05$; **$P < 0.01$; n.s., non significant, $P > 0.05$; error bars are standard errors; n=3.